

Robust Abdominal Imaging with Incomplete Breath-Holds

Nadine Gdaniec,^{1*} Holger Eggers,² Peter Börnert,^{2,3} Mariya Doneva,² and Alfred Mertins,¹

Purpose: Breath-holding is an established strategy for reducing motion artifacts in abdominal imaging. However, the breath-holding capabilities of patients are often overstrained by scans with large coverage and high resolution. In this work, a new strategy for coping with resulting incomplete breath-holds in abdominal imaging is suggested.

Methods: A sampling pattern is designed to support image reconstruction from undersampled data acquired up to any point in time using compressed sensing and parallel imaging. In combination with a navigator-based detection of the onset of respiration, it allows scan termination and thus reconstruction only from consistent data, which suppresses motion artifacts. The spatial resolution is restricted by a lower bound of the sampling density and is increased over the scan, to strike a compromise with the signal-to-noise ratio and undersampling artifacts for any breath-hold duration.

Results: The sampling pattern is optimized in phantom experiments and is successfully applied in abdominal gradient-echo imaging including water-fat separation on volunteers.

Conclusions: The new strategy provides images in which motion artifacts are minimized independent of the breath-holding capabilities of patients, and which enhance in terms of spatial resolution, signal-to-noise ratio, and undersampling artifacts with the a priori unknown breath-hold duration actually achieved in a particular scan. *Magn Reson Med* 71:1733–1742, 2014. © 2013 Wiley Periodicals, Inc.

Key words: abdominal imaging; respiratory motion; incomplete breath-hold; compressed sensing; navigator; water-fat imaging

INTRODUCTION

Respiratory motion is a common source of artifacts in magnetic resonance imaging (MRI). Performing the acquisition in a single breath-hold has proven to be an efficient means to minimize such motion artifacts, especially in abdominal imaging. However, the scan time required to cover a large volume with high-spatial resolution, as desired in abdominal imaging, often overstrains the breath-holding capabilities of patients, leading to a premature onset of respiratory motion during the acquisition and to an inconsistent dataset, which will be referred to as incomplete breath-hold. The resulting artifacts and their dependence on the acquisition order, that is the temporal order in which the k-space profiles are measured, were studied

in Ref. (1). A centric acquisition order, which covers the central k-space first, was demonstrated to reduce artifacts. This can be explained by the typical distribution of signal energy in k-space. Inconsistencies in the profiles with higher signal energy from the central k-space result in higher artifact energy, which suggests to collect these profiles first to minimize the risk of respiratory motion during their acquisition.

After the scan, the image quality is often assessed quickly, and if rated inadequate due to artifacts, the scan will be repeated with reduced spatial resolution, to adapt the scan time to the breath-holding capabilities of the particular patient. This procedure obviously complicates the workflow and prolongs the examination. Alternatively, the acquisition may be distributed over multiple breath-holds (2). This decreases the duration of each breath-hold, but increases the scan time substantially, because the patient needs several breathing cycles between subsequent breath-holds to recover. Moreover, limited reproducibility of the breath-hold position may also cause artifacts.

The breath-holding capabilities of a particular patient are unknown in advance and may degrade over multiple breath-holds, rendering the use of predefined breath-hold durations prone to failure. Performing the acquisition during free-breathing instead is attractive in particular for the examination of very sick or uncooperative subjects (3). Navigators are used to determine the breathing position and to restrict the acquisition to a certain range of breathing positions, the so-called gating window (4,5). However, this approach lowers the scan efficiency dramatically, as k-space profiles are collected in only a fraction of the breathing cycle.

Both, breath-holding and free-breathing strategies, benefit from various methods for scan acceleration. Among these, parallel imaging (PI) is particularly powerful and widely used in clinical practice. The two best-known PI methods are sensitivity encoding (6) and generalized auto-calibrating partially parallel acquisition (7). These methods permit a subsampling of k-space and estimate the missing data based on differences in the sensitivity of multiple receive coils, which need to be calibrated explicitly or implicitly for this purpose.

Compressed sensing (CS) (8,9) promises to provide further scan acceleration. It also allows a subsampling of k-space, but with the additional condition for successful reconstruction that the sampling pattern leads to incoherent aliasing. A sampling pattern, that fulfils this condition, is called an incoherent sampling pattern in the following. CS relies either on sparsity or compressibility of images. Typical sparsifying transformations applied in MRI include finite-differences and wavelet transforms (10).

This work is focused on single breath-hold abdominal imaging, which is favored to achieve a high scan efficiency and motion state consistency. It is aimed at making single

¹Institute for Signal Processing, University of Lübeck, Lübeck, Germany.

²Philips Research Europe, Hamburg, Germany.

³Department of Radiology, Leiden University Medical Center, Leiden, The Netherlands.

*Correspondence to: Nadine Gdaniec, M.S., Institute for Signal Processing, University of Lübeck, Ratzburger Allee 160, 23562 Lübeck, Germany. E-mail: gdaniec@isip.uni-luebeck.de

Received 1 February 2013; revised 8 May 2013; accepted 8 May 2013.

DOI 10.1002/mrm.24829

Published online 1 July 2013 in Wiley Online Library (wileyonlinelibrary.com).

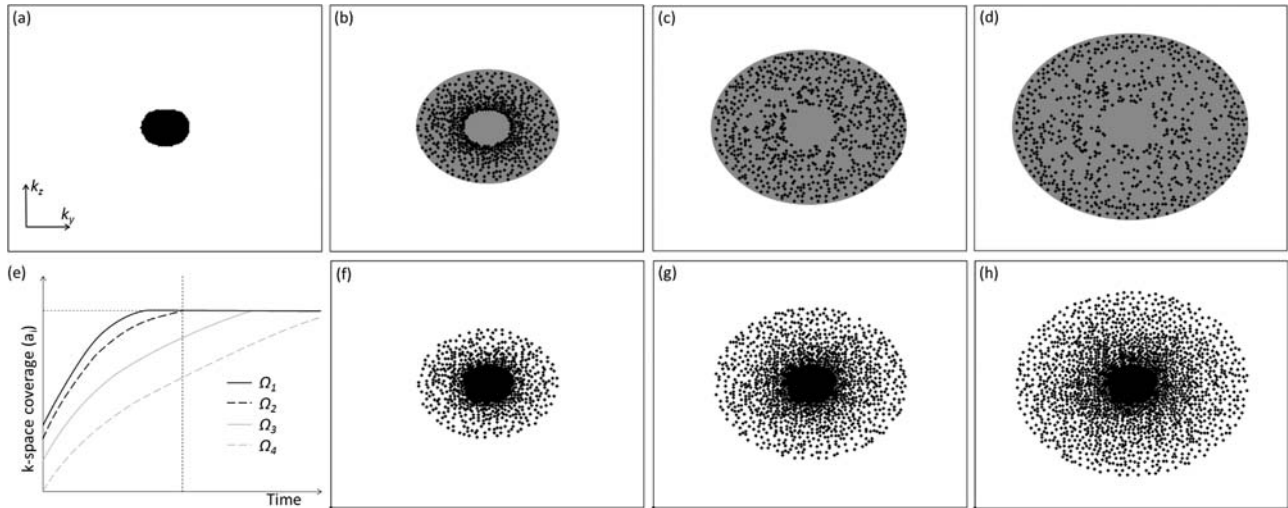


FIG. 1. Increasing spatial resolution with time. **a**: The calibration area sampled fully first. **b**: The first section, marked as gray area, and the first fraction, shown as a set of black dots, indicating phase-encoding steps to be measured. **c** and **d**: The second and third section, covering a larger k-space area and thus supporting a higher-spatial resolution, and the second and third fraction. **f-h**: All phase-encoding steps measured up to the first, second, and third fraction. **e**: The maximum $|k|$ is reached at different points in time during the acquisition for different values of Ω . Shown are schematically four graphs with $\Omega_1 > \Omega_2 > \Omega_3 > \Omega_4$. For an increasing value Ω , the target $|k|_{max}$ is reached earlier. The remaining scan time after reaching the target resolution is used to improve the signal-to-noise ratio and to reduce potential undersampling artifacts by decreasing the reduction factor.

breath-hold abdominal imaging more insensitive to incomplete breath-holds to reliably attain high image quality in most patients. PI and CS are jointly applied to cover a large volume with high spatial resolution as fast as possible. A navigator-based detection of the onset of respiration, triggering an automatic scan termination, is suggested to avoid the use of inconsistent data in the reconstruction and thus to suppress artifacts caused by incomplete breath-holds. For the first time, an acquisition order is proposed that permits an almost continuous compromise between spatial resolution and undersampling artifacts during the scan, which obviates the need for a manual, prospective adaptation of the spatial resolution or coverage to the expected breath-holding capabilities of a particular patient.

In the next section, the design of the sampling pattern and the acquisition order is explained first. Then, an outline of the employed reconstruction is given, and the performed phantom and in vivo experiments are described. Finally, the results are summarized and discussed, as are selected aspects of the new strategy for coping with incomplete breath-holds in single breath-hold abdominal imaging.

METHODS

The primary goal in the design of the sampling pattern and the acquisition order is to reconcile the different, possibly conflicting requirements resulting from the individual properties introduced above. These requirements include: (a) increasing spatial resolution over time and full uniform sampling inside a central area for autocalibrated PI, (b) nonuniform subsampling outside of the autocalibration area for CS, and (c) variable density sampling to account for the expected distribution of signal energy.

These requirements have to be met in principle throughout the acquisition to facilitate the reconstruction of images from undersampled data collected up to any point in time. Motion artifacts can thus be minimized independently of the actually achieved breath-hold duration by reconstructing from consistent data only. Moreover, these requirements permit enhancing image quality in terms of spatial resolution and undersampling artifacts continuously with the breath-hold duration.

The design of the sampling pattern and the acquisition order is described in detail in the following for three-dimensional (3D) Cartesian imaging. The acquisition order reduces to a sequence of k-space profiles in the two phase-encoding directions k_y and k_z , since the k-space is fully sampled along the read-out direction k_x .

Acquisition

Increasing Spatial Resolution and Autocalibration Area

A commonly used approach is the manual prospective adaptation of the spatial resolution or coverage to reduce the breath-hold duration. Instead, it is proposed to automatically increase the spatial resolution in the two phase-encoding directions gradually during the scan.

The k-space is divided into two parts: a central autocalibration area and the remaining k-space, which is denoted as periphery. To support an autocalibration of the sensitivity of multiple receive coils for PI, the central k-space area is fully sampled first. This is typically the most stable period of the breath-hold with the least risk of motion during the acquisition. The number of k-space profiles in this autocalibration area is denoted by N_0 . The half-axes a_0 and b_0 of the ellipse delimiting this autocalibration area define the first, coarsest spatial resolution level (cf. Fig. 1a).

Typical distributions of the signal energy in MR images have their maximum at the center of k-space and decay toward the periphery (11). Motion appearing during coverage of the central area, therefore, leads to more severe artifacts than motion appearing during coverage of the peripheral area. Because of that, the center of k-space is acquired first and the coverage of k-space is then successively increased. This approach, described in Ref. (1), is extended in this work, to allow an efficient application of PI and CS and to enable a reconstruction of images from consistent data in case of scan termination due to motion. The increase of the spatial resolution over time is described by the parameter Ω . It is defined as the inverse of the average sampling density in the covered k-space periphery and related to the temporal increase of the k-space coverage. This user-defined parameter Ω gives an upper limit of the total reduction factor ensuring that robust reconstruction can be achieved at any breath-hold duration. It thus allows trading off spatial resolution and artifact level during the acquisition. Consequently, the spatial resolution increases with the breath-hold duration, and the initially larger voxels help in attaining an acceptable signal-to-noise ratio (SNR) early on. The interpretation of Ω as reduction factor in the periphery is valid until the target resolution is reached. For later times, the reduction factor decreases.

In addition to the parameter Ω , the total reduction factor R is used in the following. R is defined as the reduction factor related to the covered k-space at a given time. As opposed to Ω , which is defined in the periphery of k-space, the total reduction factor R includes the autocalibration area.

For the generation of the profile order in the periphery, all remaining k-space profiles, apart from the central profiles, ideally to be measured are grouped into fractions. These fractions are acquired sequentially in time. A fraction is a realization of a distribution of N profiles on a section S_i of k-space. Sections are nested sets of k-space profiles, that is, each subsequent section contains all the previous sections, which can be regarded as concentric, elliptically shaped k-space areas, indicated by gray areas in Figure 1b–d. Their half-axes a_i and b_i , $i = 1, 2, 3, \dots$, determine the subsequent spatial resolution levels. The area of one section multiplied with the density of possible sample locations on a Cartesian grid ρ , which is one per unit area here, gives an estimate of the number of profiles within one section, $N_i \approx \pi a_i b_i \rho$. It has to be ensured that the average reduction factor in the periphery of section i , excluding calibration lines N_0 , is Ω

$$\frac{N_i - N_0}{iN} \approx \frac{\pi a_i b_i \rho - N_0}{iN} = \Omega. \quad [1]$$

Solving this equation for the product $a_i b_i$ yields

$$a_i b_i = (iN\Omega + N_0) \frac{1}{\pi\rho}. \quad [2]$$

Because the ratio

$$\frac{a_i}{b_i} = \frac{a_T}{b_T}, \quad [3]$$

with $a_T = |k_y|_{\max}$ and $b_T = |k_z|_{\max}$ corresponding to the target spatial resolution in the k_y and k_z direction, is fixed, the half axis can be written as

$$a_i = \sqrt{(iN\Omega + N_0) \frac{a_T}{\pi b_T \rho}}. \quad [4]$$

This is a monotonically increasing function, reaching the target resolution corresponding to a_T at some section i , which can be calculated by setting $a_i = a_T$. For larger section numbers i , the half axis $a_i = a_T$ is fixed. This can be summarized as

$$a_i = \begin{cases} \sqrt{(iN\Omega + N_0) \frac{a_T}{\pi b_T \rho}}, & \text{if } i < \frac{\pi a_i b_i \rho - N_0}{N\Omega} \\ a_T, & \text{otherwise} \end{cases} \quad [5]$$

$$b_i = a_i \frac{b_T}{a_T}. \quad [6]$$

After the target resolution is reached, any remaining time is spent on decreasing the total reduction factor, by increasing the sampling density in k-space according to the non-uniform subsampling described in the next section. The spatial resolution stays fixed, while additional samples result in decreasing reduction factors in the periphery.

The temporal evolution of a_i is schematically shown in Figure 1e for different Ω . Furthermore, Figure 1 illustrates the growing half-axes and thus the size of the sections on an example, for which $\Omega = 8$ and $N = 347$ were chosen. Each dot in the 2D k-space (two-phase-encoding directions) represents a measured profile. Added profiles from one fraction each are indicated in Figure 1a–d. As opposed to this, Figure 1f–h show the accumulated fractions, representing the resulting sampling pattern. The selection of these profiles for each fraction is explained next.

Non-Uniform Subsampling

The sampling pattern has to permit autocalibrated PI and has to lead to incoherent aliasing to support CS. This is achieved with a fully sampled autocalibration area in the center of k-space and a Poisson disk distribution (10,12) in the periphery. A Poisson disk distribution is a pseudo-random distribution of profiles with constraints, which prevent holes and clustering by defining a minimum and maximum distance between profiles. There are different methods to generate a Poisson disk distribution on a continuous grid (13), which can be mapped on a Cartesian grid. Alternatively, the coordinates of the profiles can be generated directly on a Cartesian grid with a slightly modified Poisson disk distribution, an approach that was pursued in this work. Instead of restricting the distance between profiles by a lower and an upper bound, only a lower bound r_{\min} is defined. Thus, lower distances between profiles are forbidden and the maximum distance is implicitly enforced by defining Ω and the k-space area. With the desired number of profiles and the covered k-space area, the average distance between samples can be calculated and used as a value for r_{\min} , that is, the lower bound on the distance between samples. This permits specifying only a lower bound, because a hole can only occur if clustering occurs at the same time somewhere else, and clustering is avoided by the enforced minimum distance between

samples. In case of nonautocalibrated PI, the calibration area can be skipped, but the general approach remains applicable.

The choice of random samples out of a defined and fixed set can be done with Dart-throwing (13), which subsequently chooses random samples out of the original set. If one sample was already chosen, the random selection is repeated. This immediately leads to problems for large numbers of desired samples, because repeated random selections become more frequent as the sampling density increases, which implies prohibitively long computation times. To avoid this, random selections are performed on a temporally changing subset of the original set: the set of available samples P . The profiles related to one section are unified to the subset S , which is a finite set on a Cartesian grid. The profiles are randomly chosen out of the subset $P = S \setminus (M \cup T)$, which is the set of available profiles. M is the set of already chosen profiles and with the additional definition of T , which is the set of forbidden profiles around the already chosen ones, a minimum distance-restricted distribution similar to a Poisson disk distribution can be realized as opposed to a pure random distribution. Updates of the subset P need to be performed after every random selection of a profile. If P is empty before N samples are reached, the minimum allowed distance between samples has to be decreased leading to a change of the set T . The already selected profiles of the subset M are kept, whereas new profiles are added according to the updated minimum distance.

Variable Sampling Density

The procedure described so far for generating a sampling pattern similar to a Poisson disk distribution results in a uniform sampling density. Better reconstruction results are achieved by adapting the sampling density to the expected signal energy.

The elliptically shaped central k-space area is fully sampled, and thus also captures the highest signal energy. In the peripheral k-space, the sampling density should decay as a function of the distance to the k-space center. This is achievable with a varying minimum distance r_{\min} of profiles in k-space. The variation can be a discrete distribution with constant values within specific regions or it can be made approximately continuous, which was chosen in this work. Basically, a quadratic decay of the sampling density was used in this work, which is an improvement compared to a uniform sampling density. The resulting condition for the minimum distance r_{\min} is briefly described in the following. Every profile in k-space with coordinates (k_y, k_z) can be uniquely assigned to an ellipse with fixed half-axes (a, b) , which fulfil $a/b = a_T/b_T$. The same r_{\min} is assigned to all points on the ellipse (a, b) . A linear function in the half-axis a is assumed

$$r_{\min} = ma + c = m\sqrt{k_y^2 + \left(k_z \frac{a_T}{b_T}\right)^2} + c. \quad [7]$$

The parameters m and c are determined by the constraints $r_{\min}(\frac{a_i - a_0}{2}) = \bar{r}$ and $r_{\min}(a_0) = \frac{\bar{r}}{2}$, with \bar{r} being the average distance between samples for a given Ω , leading to

$$m = \frac{\bar{r}}{a_i - 3a_0} \quad [8]$$

$$c = \bar{r} \frac{a_i - 5a_0}{2(a_i - 3a_0)}. \quad [9]$$

Because there is only a discrete set of possible distances between profiles on a Cartesian grid, the initial value of \bar{r} is the largest possible distance smaller than $\sqrt{\Omega}$. If the set of possible samples P is empty, \bar{r} is changed to the next possible lower value.

This procedure is performed to define the measured profiles, indicated by black dots in Figure 1a, within the sections.

Updates of the variable \bar{r} are required at the latest when the target resolution is reached. The additional samples keep approximating a Poisson disk distribution of profiles with increased sampling density, which corresponds to a decreased minimum distance between samples.

Acquisition Order and Motion Sensing

The process of assigning profiles to fractions was described in the last sections, but the acquisition time-order of profiles in the fractions is unaddressed and therefore discussed in this section. It can potentially be selected freely in this method, thus permitting an optimization of the trajectory in (k_y, k_z) -space.

To reduce eddy current-induced artifacts, the distance between subsequent profiles can be minimized, for instance. In this work, a different approach was used. To describe the profile ordering scheme, it is convenient to represent profiles in polar coordinates. The origin of this coordinate system is the k-space center and the radial axis points along the first phase-encoding direction k_y . The profiles from one fraction are traversed sequentially in time according to their angles in polar coordinates from lowest values to highest, which enforces an upper bound on the distance between subsequent samples and can be calculated with low computational cost.

In parallel to the data acquisition, the breath-hold has to be monitored interleaved with the data acquisition. Independent of the fractions, motion detection is performed interleaved with data acquisition after a fixed number of acquired profiles. Because of that, it is not guaranteed that the last fraction is complete after scan termination. For a low number of profiles within one fraction, this potential asymmetry in k-space sampling will not have a substantial influence on the reconstruction. For motion detection, external sensors, like belts or cameras, or internal MR-based sensors, like the pencil-beam (14,15), or other kind of navigators, can be used. In this work, a 1D pencil-beam navigator was chosen, performing 1D imaging in a small cylindrical volume to estimate the position of the diaphragm.

Reconstruction

The acquisition is stopped at the onset of breathing, and therefore, motion-free data are used for reconstruction. This prevents motion artifacts, but implies an incomplete dataset. To eliminate aliasing artifacts, a CS-PI reconstruction is applied, which deals with the potential missing

data problem. This is enabled by the incoherence of the proposed sampling pattern. The image reconstruction is performed with L1-SPIRiT (16). This reconstruction combines CS and PI based on autocalibration. As described in Ref. (17), L1-SPIRiT solves the constrained minimization problem containing the sparsifying transform Ψ , in this case a wavelet transform using unshifted Daubechies 4 wavelets,

$$\min_x \text{Joint } l_1(\Psi x) \quad [10]$$

$$s.t. \mathbf{D}\mathbf{F}x = y|_{\text{acq}} \quad [11]$$

$$\mathbf{G}y = y \quad [12]$$

via a projections onto convex sets algorithm. In this notation, $y|_{\text{acq}}$ are the acquired data in k-space, x is the image to be reconstructed, \mathbf{F} is the Fourier transform operator, and \mathbf{D} is the operator that selects the acquired data in k-space. The Joint l_1 -norm is a combined l_1/l_2 -norm, defined by $\text{Joint } l_1(\mathbf{w}) = \sum_r \sqrt{\sum_i |w_{ir}|^2}$, where i is the channel index and r is the position index of the wavelet coefficient. The joint sparsity takes into account that images from different coils have large coefficients at the same spatial positions. The first constraint enforces data consistency. The second constraint, which can also be written as

$$y_i = \sum_{j=1}^{N_c} \mathbf{g}_{ij} * y_j, \quad [13]$$

enforces calibration consistency with i, j being the channel indices and N_c being the total number of channels. The operator \mathbf{g} performs convolutions with the appropriate convolution kernels \mathbf{g}_{ij} . These calibration kernels are estimated from the fully sampled central k-space profiles.

Experiments

The proposed sampling pattern depends on the user-defined parameter Ω , which determines the trade-off between undersampling artifacts, spatial resolution, and noise level. For the evaluation of the influence of Ω on the reconstructed images as well as for a validation of the increasing spatial resolution with scan time, simulations were performed on a fully sampled 3D dataset acquired on a resolution phantom with the proposed sampling pattern. The size of the in-plane structures in this phantom was in a range of [0.5 mm; 2 mm]. The target spatial resolution of the acquisition was $0.75 \times 0.75 \times 3 \text{ mm}^3$ in a field of view (FOV) of $240 \times 240 \times 150 \text{ mm}^3$.

The data were retrospectively undersampled with the proposed sampling pattern using different number of samples to systematically evaluate the influence of the scan time on image quality. According to Eq. 5, the spatial resolution should increase with time. The image quality is not only dependent on the resolution, but also on the undersampling, which can lead to noise amplification.

Further simulations on this phantom dataset were performed for different values of Ω while keeping the total number of samples used in the reconstruction fixed. This corresponds to a fixed breath-hold duration and is indicated by the dotted vertical line in Figure 1e. The covered k-space area is determined by Eq. 5, promising increasing spatial resolution with increasing Ω . The influence of

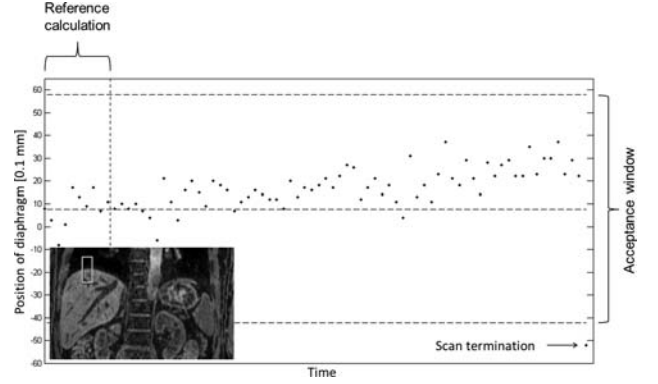


FIG. 2. Navigator signal used for automatic scan termination. The location of the 1D pencil-beam navigator is schematically shown in the inset. A typical navigator displacement signal obtained from a correlation with a reference signal is shown. A slight drift during breath-hold is visible. The first averaged navigator positions are used as reference (dotted line). An acceptance window of 10 mm width around the reference position is used as termination criterion. The navigator indicating breathing onset in this case is marked with an arrow.

Ω on the spatial resolution, as well as on the noise and undersampling artifacts, was studied.

Experiments on eight healthy volunteers, age: 30–53, were performed after obtaining informed consent, according to the rules of our institution, on a 1.5T scanner (Philips Healthcare, Best, The Netherlands) with a 3D T1-weighted spoiled bipolar dual-gradient-echo sequence, using a 16-element torso coil for signal reception and a two-point Dixon method [mDIXON (18)] for water-fat separation. The mDIXON algorithm enables a flexible choice of the echo times, which eases sequence design. The flip angle was 15° , the echo times (TEs) were 1.3 ms and 2.3 ms, the pulse repetition time (TR) was 3.7 ms, the pixel bandwidth was 1322Hz, the FOV was about $375 \times 240 \times 230 \text{ mm}^3$, and the target actual spatial resolution was $1.5 \times 1.5 \times 3 \text{ mm}^3$, covering the whole liver.

The implementation of the adaptive Poisson disk sampling pattern generation is fast enough to enable its execution directly on the scanner during protocol specification. This simplifies workflow, especially for in vivo imaging.

For imaging on volunteers, the number of fractions was 40–50, and $\Omega = 8$ was chosen.

The measurements were complemented by an interleaved navigator acquisition to detect the onset of respiration. This 1D pencil-beam navigator is normally used for gating in free-breathing acquisitions with a gating window determined in a number of breathing cycles before the actual scan. For single breath-hold acquisitions, this is impractical. Instead of determining the reference position before the breath-hold, it is derived from the first diaphragm positions of the breath-hold. The navigator is measured interleaved every 200–500 ms using a flip angle of 15° for low interference with the magnetization in the target volume. A typical navigator signal is shown in Figure 2. The reference is indicated by the dotted line and an acceptance window with a width of 10 mm around the reference position is chosen. During breath-holding, the position of the diaphragm only changes little with a slight drift.

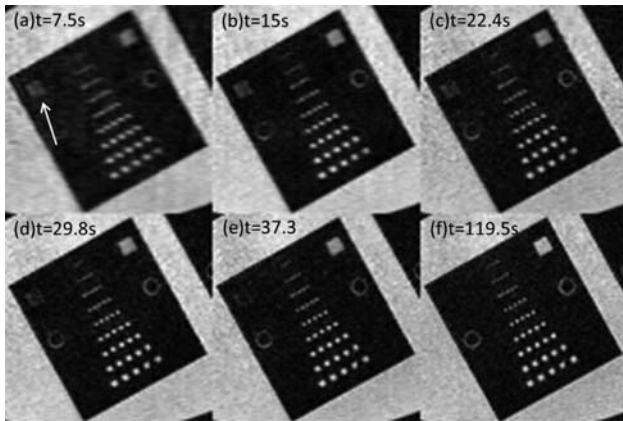


FIG. 3. Simulation of different “breath-hold” durations. A 3D phantom dataset was retrospectively undersampled using the proposed sampling pattern and a fixed Ω of 5. Different number of profiles were included in the reconstruction, simulating scan durations as indicated in **a–f**. The total reduction factor and the spatial resolution are changing with the breath-hold duration. Corresponding values (number of profiles / total reduction factor R / spatial resolution percentage) are given in the following. **a**: 1000/4.1/51, **b**: 2000/4.6/78, **c**: 3000/4.7/94, **d**: 4000/4.0/100, **e**: 5000/3.2/100, and **f**: 20480/1.0/100. The shown results are zoomed areas of slices from the resolution section of a phantom. The fully sampled dataset is shown in (f) for comparison. For increasing number of samples, the image quality improves in terms of resolution and noise.

The first navigator after onset of breathing causes scan termination approximately half a second later. The profiles acquired in this period were used for reconstruction.

The reconstruction is performed off-line so far. For faster reconstruction, a coil compression technique (19) was used before L1SPIRiT (16). The signals from the 16-channel coil were reduced to six virtual channels without significant information loss. The compressed signal was then used as an input for the CS-PI reconstruction (included in the available freeware¹), which is written in C++ and supports multiple cores of central processing units (CPUs) or graphics processing units (GPUs). In this work, a 64-bit Linux system with four CPUs (Dual-Core AMD Opteron 2220) was used, which results in reconstruction times in the order of 4–5 min for one echo. The reconstruction times of this algorithm for multiple CPUs and GPUs were studied in detail by Murphy et al. (20). The resulting images from the individual coils were combined using a Roemer et al. reconstruction (21) to obtain one complex valued image for each of the two echoes. To these two echo images, the mDIXON algorithm was optionally applied, resulting in one water and one fat image.

Feasibility was shown on different volunteers for different breath-hold durations. One of the in vivo datasets was further analyzed by retrospectively simulating shorter breath-hold durations. This allows a comparison without misregistration artifacts from multiple breath-holds.

To illustrate the effectiveness of motion suppression with the proposed method, a series of experiments on one volunteer with different breath-hold durations was

additionally performed. The scans were terminated after a fixed duration of 20 s. Reconstruction was performed from data acquired before onset of breathing only and from all acquired data.

RESULTS

Results from simulations using a fixed Ω of 5 are shown in Figure 3 for increasing number of samples. These results mimic measurements terminated at varying scan progress, with scan durations indicated in the images. As expected, the resolution in AP direction (in-plane) and the through-plane resolution improve and undersampling artifacts vanish with growing number of samples. The read-out direction points from left to right and therefore, the resolution in this direction stays fixed. The improved in-plane resolution can be deduced from reduced blurring for increasing number of samples as well as from the structures in the resolution phantom. The improved through-plane resolution becomes obvious when comparing results with the fully sampled reference dataset in Figure 3f. In the upper left corner, a high intensity square (see arrow) from a neighboring slice appears in the undersampled data, which is absent in the original image. The intensity reduces for increasing number of samples, which reflects the improved through-plane resolution.

An important parameter for the generation of the proposed sampling pattern is Ω . It determines the velocity with which the k -space area is covered over time and affects the reconstruction artifacts and the SNR at the same time. Reconstruction results from the same phantom dataset are shown in Figure 4. It is retrospectively undersampled for

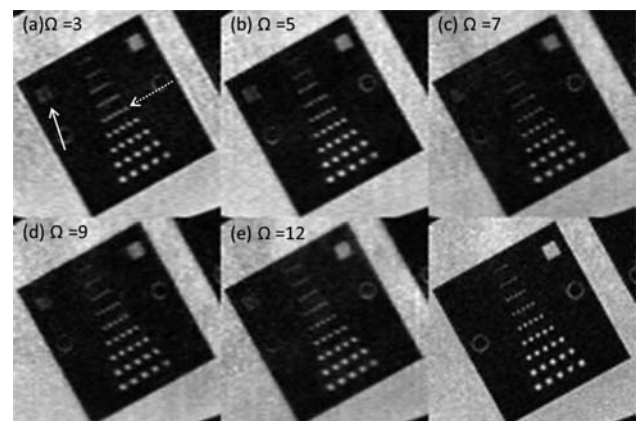


FIG. 4. Simulation of different values of the parameter Ω . A 3D phantom dataset was retrospectively undersampled, using the proposed sampling pattern and a fixed amount of data (2000 profiles). The chosen values for the parameter Ω are indicated in the images, resulting in different total reduction factors and spatial resolution. Corresponding values (total reduction factor R / spatial resolution percentage) are given in the following. **a**: 2.83/61, **b**: 4.58/78, **c**: 6.42/91, **d**: 7.92/100, and **e**: 7.92/100. The shown results are enlargements of the resolution section of the phantom. The result for full sampling is shown in f for comparison. The achieved spatial resolution depends on the reconstruction and improves from (a–c) (see dotted arrow for in-plane and full arrow for through-plane resolution). On the other hand, images with large values of Ω (d,e) suffer from image artifacts and increased noise, which restricts the range of acceptable values of Ω .

¹<http://www.eecs.berkeley.edu/~mlustig/Software.html>

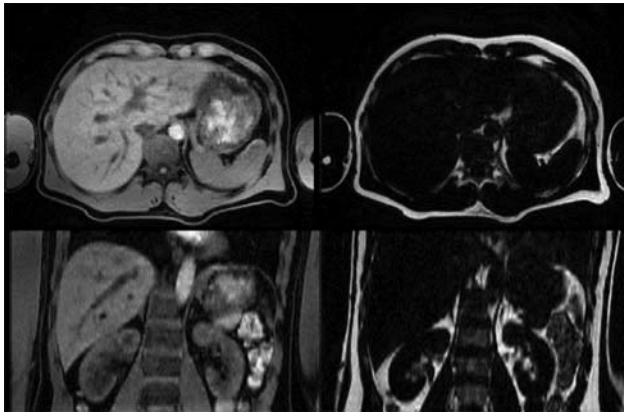


FIG. 5. Results in a volunteer from a scan with 16 s breath-hold duration. This corresponds to a total reduction factor of $R = 4.14$ related to the achieved k-space coverage $|k|_{\max}$ at scan termination. Example slices of water and fat images in the axial and the reformatted coronal plane are shown. Images indicate good image quality and 3D coverage without motion artifacts.

different values of Ω and a fixed value of samples $N = 2000$, which corresponds to a fixed scan duration. The values of Ω are indicated in the images. It can be seen in Figure 4a–c that the in-plane as well as the through-plane resolution

increase. The increased in-plane resolution is visible in the line marked with the dotted arrow. In Figure 4a, it appears as a line, whereas it appears as a set of dots in Figure 4c. The tendency of improved through-plane resolution is also visible in the left corner (see full arrow), where a neighboring slice becomes visible in the undersampled data. The intensity becomes lower in Figure 4c compared to Figure 4a. For higher Ω , resulting images given in Figure 4d,e, the image quality is starting to degrade by a higher noise level, because the sampling density is too low in the periphery.

The proposed sampling pattern was evaluated in healthy volunteers yielding good image quality. Reconstructed images from a scan with flexible scan termination after 16 s, which is a moderate breath-hold duration, are shown in Figure 5. The reformatted water and fat images in the axial and coronal plane show good image quality without artifacts from respiratory motion.

The measurement underlying Figure 6 was automatically stopped at the onset of breathing after 19 s. For comparison, shorter breath holding was simulated by retrospectively skipping data. Toward shorter acquisition times, the spatial resolution of the water and fat as well as of the single echo images is reduced in the two phase-encoding directions, which are anterior-posterior and feet-head. The corresponding difference images of the first echo in the

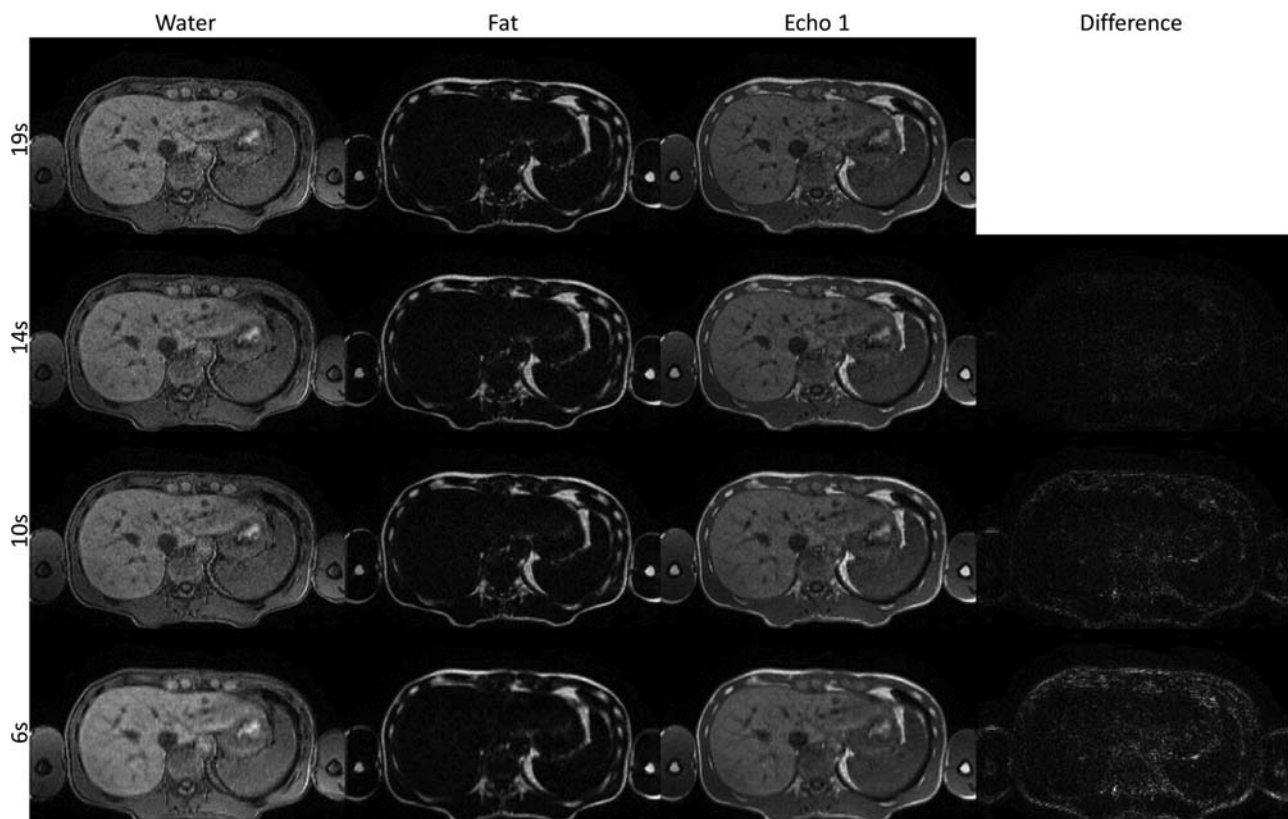


FIG. 6. Influence of breath-hold duration on image quality. The underlying measurement was automatically stopped after 19 s at breathing onset. For a comparison without misregistration artifacts data were retrospectively discarded to simulate shorter breath-hold durations of 14 s, 10 s and 6 s. Images of a selected slice of the 3D datasets are shown. The water- and fat-only image, the first echo image and the difference of this image to the first echo image obtained with the 19 s breath-hold, upscaled by a factor of three, are shown. A lower spatial resolution, both in-plane and through-plane, becomes apparent for shorter breath-hold durations.

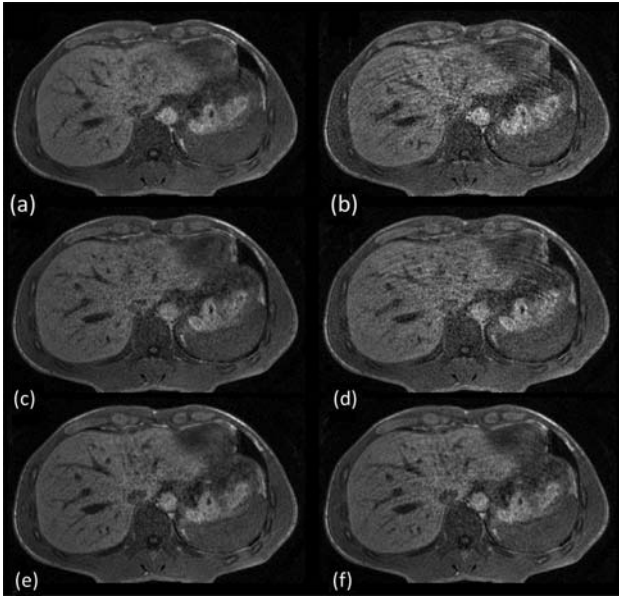


FIG. 7. Motion artifact suppression by scan termination. Reconstructed images from the first echo of a dual-echo acquisition for three individual scans using the proposed sampling pattern with a total duration of 20 s ($R = 2.8$) without self-termination and incomplete breath-holds of **a,b**: 12 s ($R = 4.5$), **c,d**: 15 s ($R = 3.8$), and **e,f**: 18 s ($R = 3.1$) duration. (a,c,e) are reconstructed from data acquired before onset of breathing, and (b,d,f) from all data acquired in the first 20 s while the reconstruction parameters were kept the same in all cases. Motion artifacts are clearly visible in (b,d,f), significantly degrading image quality.

fourth column, upsampled by a factor of three, demonstrate once again the loss of in-plane and through-plane resolution for shorter breath-holds. Difference images of the water and fat images were calculated as well, showing similar result.

The measurements underlying Figure 7. were stopped after a fixed scan duration of 20 s. The volunteer started breathing already after 12 s (Fig. 7a,b), 15 s (Fig. 7c,d), and 18 s (Fig. 7e,f) respectively. Figure 7a,c,e show images reconstructed from data acquired before breathing onset, while Figure 7b,d,f show images reconstructed from all acquired data. Although the data are acquired with the proposed sampling pattern, which is already less sensitive to motion, (b,d,f) are degraded by severe motion artifacts. As opposed to this, no motion artifacts are visible in (a,c,e) from the same datasets, because they were reconstructed only from consistent data.

DISCUSSION

Imaging of the abdomen often suffers from motion artifacts. Therefore, a novel approach for more robust 3D abdominal imaging with incomplete breath-holds was proposed and feasibility was shown in simulations and in vivo measurements. Good image quality was obtained for the single-echo and the water-fat images for all breath-hold durations albeit at different spatial resolutions. Motion artifact suppression by scan termination was clearly shown to

be superior to using inconsistent data for reconstruction (cf. Fig. 7). This approach ensures an optimal compromise between undersampling artifacts and spatial resolution for an arbitrary breath-hold duration, while preventing motion-induced artifacts. Instead of adapting the spatial resolution in advance, based on an estimate of the breath-hold duration a particular patient is able to achieve, it is automatically increased during the scan. This is advantageous because the breath-hold duration of a patient is difficult to predict, especially for sick or uncooperative patients, and in any case potentially diagnostically useful images can be obtained making undesired scan repetitions unnecessary.

In the previously proposed approach by Maki et al. (1), the acquisition is not terminated and the complete dataset is used for reconstruction. This ensures full resolution, but leads to motion artifacts, dependent on the breath-hold duration. A simple extension of the previous method would be the combination with a motion sensor for scan termination. This would result in lower resolution than in the approach proposed here, which integrates PI and CS and therefore enables undersampling of k -space.

The main parameters for the generation of the sampling pattern are the number of calibration lines in the center of k -space, the number of fractions f , and Ω . The number of calibration lines is mainly determined by the reconstruction and the energy of the signal. In the reconstruction technique used in this work (L1SPIRiT), a convolution kernel fit is performed from the calibration lines. A sufficient number of equations is needed for this optimization process. Therefore, an increasing number of calibration lines up to a certain limit leads to an improved calibration kernel. Furthermore, it is advantageous if the part of the signal with highest energy is fully sampled. However, with increasing number of calibration lines, the time to acquire the lines is also increased, leading to lower-spatial resolution. For the selection of a suitable number of fractions, two competitive factors, acquisition time of one fraction and distance between samples, have to be taken into account. An incomplete fraction results in an asymmetrically acquired k -space, which is less severe if the number of samples within one fraction is low. This makes a large number of fractions preferable. On the other hand, a larger number of samples in one fraction results in reduced average distance between samples, and therefore, in reduced eddy currents. The potential asymmetry in k -space is caused by the chosen temporal order within the fractions according to the angle in polar coordinates of the profiles. Improvements can be achieved if the profiles within one fraction are traversed in a manner similar to a spiral. Another possibility is to choose the same number of profiles in a shot as in one fraction, which ensures a symmetric sampling pattern. This potentially comes at the cost of lower-temporal resolution of the motion sensing or of a higher distance between samples.

The evolution of the covered k -space area is determined by the parameter Ω through Eq. 5. This evolution together with the reconstruction determines the spatial resolution and the artifact level, which are competitive. To determine the reasonable range for Ω , simulations were performed on a retrospectively undersampled phantom scan.

As expected from Eq. 5, the resolution improves for increasing Ω . At some stage, residual undersampling artifacts and noise arise, which can not be removed by the reconstruction and become clearly visible for $\Omega = 12$. Therefore, as a compromise, $\Omega = 8$ was chosen for the experiments. This choice is specific for the chosen coil and sequence, which potentially needs to be slightly adapted for other configurations.

The chosen variable density is only slightly adapted to the expected signal distribution in k-space. It is decaying to the k-space periphery, which is an improvement compared with uniform sampling density. This choice for the sampling density, as implicitly given in Eq. 7, is just one possibility and can potentially be changed to an arbitrary function. Optimization could lead to further improved reconstruction results. Furthermore, in this work, the forbidden samples are derived from a circular neighborhood with radius r_{\min} around the measured samples. This can potentially be replaced by an elliptical neighborhood, which supports different undersampling factors in the two phase encoding directions.

Once the maximum resolution is reached, the remaining scan time is used to reduce artifacts by decreasing the effective reduction factor and improving SNR, until the patient starts to breathe. The acquisition adapts to the actually achieved breath-hold duration, which can be monitored either by external sensors or navigators, or can be determined from a series of images reconstructed from different amounts of data. With the chosen 1D pencil-beam, a robust termination method was implemented. Scan termination is favorable compared to an image-based criterion applied retrospectively, because of patient comfort and scan efficiency. However, the chosen navigator has the disadvantage of interrupting the steady state of the magnetization in the imaging volume. Because of that, the intershot signal intensity varies resulting in contrast variations. Furthermore, the navigator can lead to magnetization saturation in the imaging volume. The use of motion detection based on repeatedly measuring the k-space center could avoid the corresponding artifacts (22).

The results and the image quality are promising, and current work is directed toward an online reconstruction to allow a clinical evaluation.

The single-echo images are reconstructed independently of each other in this study, instead of performing a joint CS reconstruction and water-fat separation (23–25). As discussed in Ref. (23), the advantage of applying a joint CS reconstruction and water-fat separation grows with the number of echoes, both because of the increased spectral dimension and the improved model accuracy. The reason for focusing in this work on a sequential CS reconstruction and water-fat separation is that the improvement expected from a joint CS reconstruction and water-fat separation is small for a two-point water-fat separation and hardly justifies the additional complexity.

The presented approach is not restricted to gradient-echo sequences and can potentially be applied also to other sequences and contrasts. For this purpose, the acquisition order within the fragments needs to be adapted to match the imaging conditions for the particular sequence.

CONCLUSIONS

Breath-holding is a very efficient strategy for imaging of the abdomen if patients can hold their breath for the whole scan. Premature onset of breathing leads to motion artifacts and, therefore, has adverse effects on image quality. The proposed sampling pattern results in temporally increasing spatial resolution and enables flexible scan termination at onset of breathing. This method preserves the benefits of breath-holding, while suppressing motion artifacts.

Simulations on phantom data were performed for an optimal choice of key parameters of the proposed sampling pattern, and the feasibility of the overall concept was demonstrated in volunteer experiments. The sampling pattern was successfully applied to 3D gradient-echo imaging of the abdomen and extended to dual-echo imaging for water-fat separation.

REFERENCES

- Maki JH, Chenevert TL, Prince MR. The effects of incomplete breath-holding on 3D MR image quality. *J Magn Reson Imaging* 1997; 7:1132–1139.
- Feinberg DA, Rofsky NM, Johnson G. Multiple breath-hold averaging (MBA) method for increased SNR in abdominal MRI. *Magn Reson Med* 1995; 34:905–909.
- Azevedo RM, Campos ROP, Ramalho M, Herédia V, Dale BM, Semelka RC. Free-breathing 3D T1-weighted gradient-echo sequence with radial data sampling in abdominal MRI: preliminary observations. *AJR* 2011; 197:650–657.
- Vasanawala SS, Iwadate Y, Church DG, Herfkens RJ, Brau ACS. Navigated abdominal T1-w MRI permits free-breathing image acquisition with less motion artifacts. *Pediatr Radiol* 2010; 40:340–344.
- Runge VM, Clanton JA, Partain CL, James AE. Respiratory gating in magnetic resonance imaging at 0.5 T. *Radiology* 1984; 151:521–523.
- Pruessmann KP, Weiger M, Scheidegger MB, Boesiger P. SENSE: sensitivity encoding for fast MRI. *Magn Reson Med* 1999; 42:952–962.
- Griswold MA, Jakob PM, Heidemann RM, Nittka M, Jellus V, Wang J, Kiefer B, Haase A. Generalized autocalibrating partially parallel acquisitions (GRAPPA). *Magn Reson Med* 2002; 47:1202–1210.
- Donoho DL. Compressed Sensing. *IEEE Trans Info Theo* 2006; 52:1289–1306.
- Candes E, Romberg J, Tao T. Robust uncertainty principles: exact recovery from highly incomplete Fourier information. *IEEE Trans Info Theo* 2006; 52:489–509.
- Lustig M, Donoho D, Pauly JM. Sparse MRI: The application of compressed sensing for rapid MR imaging. *Magn Reson Med* 2007; 58:1182–1195.
- Fuderer M. The information content of MR images. *IEEE Trans Info Theo* 1998; 7:368–380.
- Yellott JI. Spectral consequences of photoreceptor sampling in the rhesus retina. *Science* 1983; 221:382–385.
- Dunbar D, Humphreys G. A spatial data structure for fast Poisson-disk sample generation. *Proc SIGGRAPH* 2006; 503–508.
- Pauly J, Nishimura D, Macovski A. A k-space analysis of small-tip-angle excitation. *J Magn Reson Imaging* 1989; 81:43–56.
- Nehrke K, Börner P, Groen J, Smink J, Böck JC. On the performance and accuracy of 2D navigator pulses. *Magn Reson Med* 1999; 178:1173–1181.
- Lustig M, Alley M, Vasanawala S, Donoho DL, Pauly JM. 11-SPiRiT: autocalibrating parallel imaging compressed sensing. In Proceedings of the 17th Annual Meeting of ISMRM, Honolulu, Hawaii, USA, 2009. p. 379.
- Vasanawala SS, Alley MT, Hargreaves BA, Barth RA, Pauly JM, Lustig M. Improved pediatric MR imaging with compressed sensing. *Radiology* 2010; 256:607–616.
- Eggers H, Brendel B, Duijndam A, Herigault G. Dual-echo Dixon imaging with flexible choice of echo times. *Magn Reson Med*, 2011; 65:96–107.
- Zhang T, Pauly JM, Vasanawala SS, Lustig M. Coil compression for accelerated imaging with Cartesian sampling. *Magn Reson Med* 2013; 69:571–582.

20. Murphy M, Alley M, Demmel J, Keutzer K, Vasanawala S, Lustig M. Fast l1-SPIRiT compressed sensing parallel imaging MRI: Scalable parallel implementation and clinically feasible runtime. *IEEE Trans Info Theo* 2012; 31:1250–1262.
21. Roemer PB, Edelstein WA, Hayes CE, Souza SP, Mueller OM. The NMR phased array. *Magn Reson Med* 1990; 16:192–225.
22. Brau ACS, Brittain JH. Generalized self-navigated motion detection technique: Preliminary investigation in abdominal imaging. *Magn Reson Med* 2006; 55:263–270.
23. Doneva M, Börnert P, Eggers H, Mertins A, Pauly J, Lustig M. Compressed sensing for chemical shift-based water-fat separation. *Magn Reson Med* 2010; 64:1749–1759.
24. Sharma SD, Hu HH, Nayak KS. Accelerated water-fat imaging using restricted subspace field map estimation and compressed sensing. *Magn Reson Med* 2011; 67:650–659.
25. Wiens CN, McCurdy CM, Willig-Onwuachi JD, McKenzie CA. R2*-corrected water-fat imaging using compressed sensing and parallel imaging. *Magn Reson Med* 2014; 71:608–616.